Article

Performance of a Nozzle to Control Bath Level Oscillations and Turbulence of the Metal-Flux Interface in Slab Molds

María Guadalupe González-Solórzano [1,*]**, Rodolfo Davila Morales** [1]**, Javier Guarneros** [2]**, Carlos Rodrigo Muñiz-Valdés** [3] **and Alfonso Nájera Bastida** [4]

[1] Department of Metallurgy, Instituto Politécnico Nacional-ESIQIE, Mexico City 07738, Mexico; rmorales@ipn.mx
[2] K&E Technologies, Mexico City 07365, Mexico; 201520457@tese.edu.mx
[3] Facultad de Ingeniería, Universidad Autónoma de Coahuila, Arteaga 25350, Mexico; rodrigo.muniz@uadec.edu.mx
[4] Metallurgy Engineering, Instituto Politécnico Nacional-UPIIZ, Zacatecas 98160, Mexico; anajerab@ipn.mx
* Correspondence: mgonzalezs2007@alumno.ipn.mx

Abstract: The characterization of the turbulent flow of liquid steel in a slab mold using a commercial nozzle was carried out through physical experiments and mathematical models. Six ultrasonic sensors were located at each side of the nozzle to obtain real-time plotting of the bath levels during the experimental time. An ultrasonic transducer located in the mold, 20 mm below the meniscus, determines the velocities and the turbulent variables along with the distance from the narrow face to the position of the nozzle's outer wall. These data, together with the mathematical simulations, demonstrated a high correlation of bath level oscillations and the time-dependent behavior of the discharging jets. The flow inside the mold shows low-frequency non-symmetric patterns without a severe turbulent in the meniscus. The source of this instability is the partial opening of the slide valve gate used to control the mass flow of liquid.

Keywords: bath levels oscillations; metal-flux interface; flux entrainment; meniscus velocity

1. Introduction

The fluid flow of liquid steel in continuous casting molds is critical to cast high-quality slabs. The fluid flow pattern should include double roll flows, one upper and the other lower at both sides of the mold, to guarantee flow symmetry and uniform heat transfer conditions. Controlled thermal gradients in the narrow and broad faces of the mold permit the formation of a solidified shell with a strength large enough to support the liquid core [1,2]. Feeding in the mold-strand gap a lubricating flux decreases the friction forces between this shell and the mold walls. The casting process's three other essential variables are the bath level in the mold, the liquid metal speed, and flux melting rate at the metal-flux interface. The uncontrolled liquid flow near the metal-flux interface will usher powder entrainment to become trapped particles in the solidified shell. Non-melted powder induces sticking breakouts and bath level oscillations to promote transversal slab depressions and strand breakouts [3–6]. The literature in the field dealt with the effects of nozzle immersion depth, casting speed, steel grade, and thermo-solute convection on the fluid patterns of liquid steel in slab molds [7–12]. However, fluid flow in the nozzle is probably the most important tool to provide fluid flow patterns that fulfill the requirements mentioned here.

The importance of nozzle design on the fluid flow control of liquid steel has been recognized as a critical factor in slab quality [13–15], especially when slivers are frequent in the cast slabs. Specifically, a criterion establishes that the maximum melt velocity of 0.3 m/s at the melt surface, for any given casting speed, avoids flux entrapment and the derived generation of slivers [16,17]. In other words, the metal-slag interface is under the effects of shear stresses originated by the upper roll flow causing waves, leading to instabilities of

the top phase into the lower steel phase. Once reaching a critical shear stress and a corresponding interfacial fluid velocity these instabilities derive into traveling droplets flowing inside the liquid metal. These slags droplets will, eventually, form nonmetallic inclusions in the semifinished product, yielding a dirty final product. Hence, their elimination is a requirement for casting clean steel. However, this criterion for maximum melt velocity might be small, deriving into the transport of cold steel to the melt meniscus with a sensible heat that is not large enough to melt down the lubricator flux. Moreover, cold steel in the meniscus level will eventually solidify, creating strand breakouts conditions [18–20]. Other researchers reported that higher velocities of the melt in the meniscus than 0.3 m/s ensure suitable flux melting rates without entrainment of flux into the melt bulk [21,22]. Industrial experience indicates that a hot meniscus ensures a better slab surface, with smaller number of defects, such as slivers, cracks, slag entrapment, and transversal depressions [23,24]. Therefore, a suitable nozzle design working for some given specific conditions must deliver discharging jets yielding symmetric, double roll flows, hot steel at the meniscus level, and controlled turbulence leading to minimum velocity spikes along the casting time [22].

A commercial nozzle operating in a steel company located in the USA (see Figure 1a) yields slabs with high-quality surfaces and evidence of well-controlled friction forces between the mold and the shell, observing an overall good operation. Given these characteristics, an interest emerged to understand the reasons supporting the excellent performance of this nozzle and finding the design principles leading to successful casting processes. Therefore, the present research aims to characterize the turbulent flow of liquid steel in a slab mold using the nozzle in Figure 1a through physical experiments and mathematical models.
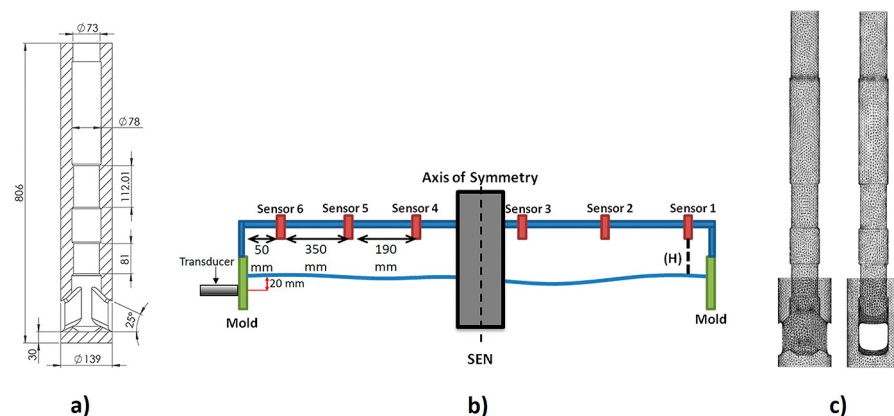

Figure 1. The nozzle and the experimental setup. (**a**) Geometric features of the industrial nozzle (mm). (**b**) The mold model equipped with meniscus levels sensors and the ultrasonic transducer to measure turbulence. (**c**) Interior wall of the nozzle.

2. Experimental Work

The physical model employs a 1:1 water model scale of a slab caster made of transparent plastic sheets. The dimensions of the mold are 1450×235 mm^2, the casting speed is 1.4 m/min, the equivalent flow rate is 7.95×10^{-3} m^3/s, and the nozzle immersion (measured from the upper edge of the port to the meniscus level) is 120 mm. The model fulfills the criteria of Reynolds and Froude numbers for scaling up liquid steel flow by using water; the surrounding pressure is 10,1325 Pa. The plastic mold has a height of 1700 mm, of which 200 mm remain immersed in a sealed tank filled with water. In the interior of the tank, an immersed pump elevates the liquid to an upper tundish to maintain a constant bath level of 1 m. A valve and a flow meter inserted in the vertical pipe, transporting water from the tank to the tundish, control the water flow. Below the top of the upper tube nozzle (UTN), a replica of the actual sliding gate valve (SGV) of this caster is made of plastic to control water flow to the mold. Six ultrasonic sensors, three located at each side of the nozzle, placed 120 mm above the static level of the water bath, capture the analogic signals of the variations of the meniscus level during the experimental time. A data acquisition

card converts these analogic signals into digital ones permitting an on-real time plotting of the bath levels during the measuring time. To capture the general feature of the flow, a red dye tracer, consisting of an aqueous solution of a food colorant, is injected by a syringe through a drill performed in the UTN, sealed with a rubber plug.

Another drill practiced in the midface of one of the narrow faces, located 20 mm below the water meniscus, holds an ultrasonic transducer of 10 million Hertz that receives the signals of the liquid's motion. The signals of the ultrasonic transducer are transformed into digital signals and processed through software to determine the velocities and the turbulent variables along with the distance from the narrow face to the position of the nozzle's outer wall. Figure 1b shows a simplified scheme of the experimental setup. Figure 1c shows a solid version of the interior walls of the nozzle drawn through a computational mesh.

The experimental procedure consists of fixing the water flow rate manipulating the valve and the flow meter readings installed in the vertical pipe, and maintaining the fixed bath level in the tundish. The slide gate opening corresponds to the desired casting speed reported equivalent to a flow area of 2.57×10^{-3} m^2. Once starting the closed-loop of the water flow, the system works for 15 min to attain steady-state conditions of the meniscus levels, corresponding to the turbulent flow conditions. At an arbitrary time, meniscus levels and turbulence measurements start storing all acquired data in a computer. Once all measurements conclude, the tracer is injected, and a conventional video camera records the images of its mixing kinetics. Although it is evident that a water model does not reproduce faithfully the current flows in slab molds, the overall flow patterns in casting systems will follow those reported here.

3. The Mathematical Model

The mathematical simulations consist of an Unsteady Reynolds-Averaged Navier Stokes (URANS) computational scheme based on the realizable *k-ε* model [25] to complement the experimental work described above. The simulations ensure that the fluid of water is in line with the experimental measurements described above. The realizable *k-ε* turbulence model is simple, contains an alternative formulation for the turbulent viscosity, and predicts the boundary layer characteristics under large pressure gradients. Additionally, the realizable model provides the best performance of all the *k-ε* model versions for several conditions of separated flows and flows with complex secondary flow features. The equations governing the motion of an incompressible fluid include one equation for continuity and three equations for momentum transfer expressed by averaged on time according to the Reynolds decomposition ($u_i = u_i + \overline{u}_i$):

$$\frac{\partial \overline{u}_i}{\partial x_i} = 0 \tag{1}$$

$$\frac{\partial \overline{u}_i}{\partial t} + \frac{\partial \left(\overline{u}_i \overline{u}_j \right)}{\partial x_j} = -\frac{1}{\rho} \frac{\partial p}{\partial x_i} + \nu \frac{\partial^2 \overline{u}_i}{\partial x_i \partial x_j} + \frac{1}{\rho} \frac{\partial \tau_{ij}^R}{\partial x_j} + \rho g_i \tag{2}$$

The Reynolds stresses, $\tau^R = -\overline{u_i' u_j'}$ is approximated through the hypothesis of the eddy viscosity, μ_t, according to the Boussinesq expression:

$$\tau_{ij}^R = 2\mu_t S_{ij} - \frac{2}{3} k \delta_{ij}, \tag{3}$$

where S_{ij} is the mean deformation rate tensor. The relation between the eddy or turbulent viscosity and the kinetic energy ($k = \frac{1}{2}\overline{u_i' u_j'}$) and its dissipation rate ε is:

$$\nu_t = \frac{C_\mu k^2}{\varepsilon} \tag{4}$$

where C_μ is not a constant; it is a function of the mean strain and rotation rates, the angular velocity of the system rotation, and the turbulence field ($C_\mu = \frac{1}{A_0 + A_s \frac{kU^*}{\varepsilon}}$). The model simulates the fields of the kinetic energy and its dissipation rate to calculate the eddy viscosity, by solving the k and ε balances:

$$\frac{\partial k}{\partial t} + \nabla \cdot (\overline{u}k) = \tau^R : \nabla \overline{u} - \varepsilon + \nabla \cdot \left[\left(\nu + \frac{\nu_t}{\sigma_k} \right) \nabla k \right] \tag{5}$$

$$\frac{\partial \varepsilon}{\partial t} + \nabla \cdot (\overline{u}\varepsilon) = C_{\varepsilon 1} \frac{\varepsilon}{k} + C_1 S_{ij} \varepsilon - C_{\varepsilon 2} \frac{\varepsilon^2}{k + \sqrt{\nu \varepsilon}} + \nabla \cdot \left[\nu + \frac{\nu_t}{\sigma_\varepsilon} \right] \nabla \varepsilon \tag{6}$$

where $C_1 = \max \left[0.43 \frac{\eta}{\eta + 5} \right]$, $\eta = S \frac{k}{\varepsilon}$, $S = \sqrt{2S_{ij}S_{ij}}$, and $C_{\varepsilon 1} = 1.44$, $C_{\varepsilon 2} = 1.9$, $\sigma_k = 1.0$, $\sigma_\varepsilon = 1.2$. The no-slipping boundary condition applies to all walls in the system, and the link between the wall and the outer flow, from the boundary layer, is through the log-wall function [26]. The boundary condition of the velocity inlet is calculated by an energy balance using Bernoulli's Equation, applied from the bath surface in the tundish to the UTN. The shear boundary condition applies on the bath surface, to take into account the presence of the upper layer phase. The present model is focused on the simulation of the water model experiments. In the outlet, a pressure boundary condition governs the exit of the fluid outside the mold.

In the discretization of the governing Equations, a Second-Order Upwind method was employed [27]. The Green-Gauss-based model approximates the derivatives in the cell centroid, the body force weighted approach works to compute the pressure field. The computing unstructured-tetrahedral mesh consists of 2,591,343 cells and 486,328 nodes. The averaged skewness of the computing mesh is 0.20588 with a standard deviation of 0.01652. The averaged orthogonal quality of the mesh is 0.88292 with a standard deviation of 8.713×10^{-2}. The PISO algorithm helps to make the pressure-velocity coupling. The sum of all residuals of the flow variables smaller than 10^{-4} establishes the convergence criterion of the numerical computations.

The solution of the motion equations provides the velocity fields using a previously calculated, or assumed, pressure field. These velocity fields employed in Equations (5) and (6) permit the calculation of the k and ε fields which, once substituted, in Equation (4), yields the field of the eddy viscosity. The procedure requires an iterative process, provided by the PISO algorithm, using as the convergence criterion the fulfillment of the mass balance provided by the Equation of continuity, expressed through the pressure field.

4. Results and Discussion

Figure 2a–c shows the tracer mixing characteristics at 0.5, 1.5, and 4.5 s, respectively, after its injection in the UTN. The right jet leaves the nozzle with apparently larger velocity than the left one as the tracer has advanced a longer distance, as seen in Figure 2a. Figure 2b confirms the observation mentioned above since, as seen, the right jet has impacted the narrow face, and the upper roll flow is about to be revealed. Figure 2c shows the upper and lower flows well developed at both sides of the nozzle. Figure 2d shows a selected image, derived from the files of the mathematical simulations, resembling, as close as possible, the trajectory of the tracer. The results in Figure 2a–d shows good qualitative matching between the flow in the mold and the mathematical model results.
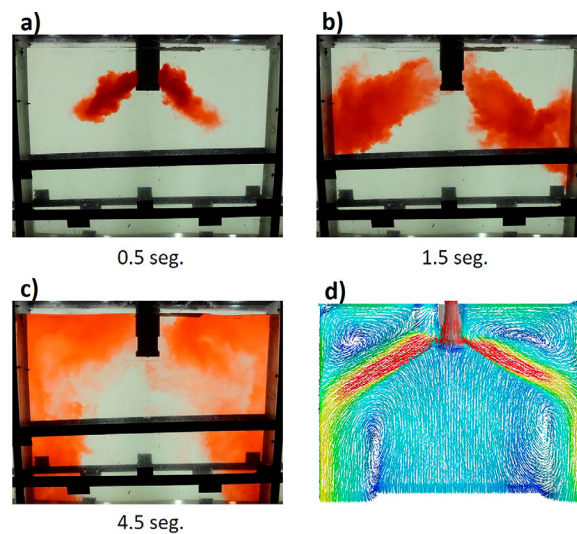
Figure 2. Tracer mixing in the mold model: (**a**) 0.5 s after injection, (**b**) 1.5 s after injection, (**c**) 4.5 s after injection. (**d**) Numerical velocity field.

Figure 3a–c shows the variations of the meniscus levels recorded by the six ultrasonic sensors organized by their corresponding symmetric positions. There is a slight mismatch between bath levels in the mold corners (sensors 1 and 6); see Figure 3a. The region located between the narrow face and the nozzle features the largest velocities of the upper roll flow and the best matching of the bath level variations reported by sensors 2 and 5 (see Figure 3b). Finally, sensors 3 and 4 yield a slight mismatching of meniscus level variations. The close overlapping of the meniscus level variations between the equivalent positions of the measuring positions in the right and left sides indicate that the nozzle provides a permanent general symmetric flow. The statistical covariances of the bath levels among the six positions of measurements provide further verification of the flow symmetry using the fundamental identity $Cov\left(X_i X_j\right) = Cov\left(X_j X_i\right)$. Figure 3d shows positive and large covariances for the six positions of meniscus level variations, and the covariance increases from the mold corners to the central distance between the narrow face and the nozzle and adjacent positions to the nozzle.
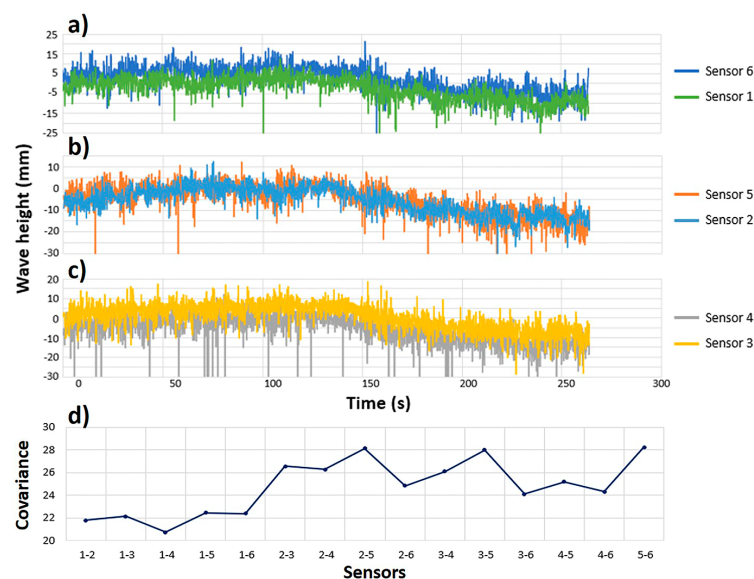

Figure 3. Variations of meniscus level and their covariances: (**a**) Sensors 1 and 6, (**b**) Sensors 2 and 5, (**c**) Sensors 3 and 4. (**d**) Covariances of bath level fluctuations.

The instantaneous variations of the upper of upper roll flows, going from the narrow walls toward the nozzle, must provide a quantitative idea about the flow dynamics. Indeed, Figure 4a,b shows the time-varying velocity profiles, calculated through the mathematical model, along a line traced from the narrow wall to the nozzles' wall (20 mm below the meniscus surface, i.e., the same position of the ultrasonic transducer). The numbers in the plots indicate the times corresponding to the smallest and largest velocity profiles. The numbers in the color-scale of Figure 4a,b indicates the flow times in seconds when these velocity profiles are determined and make evident their radical changes for periods of only five seconds. The velocity variations go from 0.15 to 0.55 m/s, and this upper limit exceeds the conventional limit of 0.3 m/s to supposedly avoid flux entrapment. However, choosing the physical properties of the lubricating flux is possible to avoid or at least decrease the danger of slag entrainment. For example, take a 305 stainless steel with a chemistry of 0.05% C, 0.02% Si, 1.24% Mn, 17.1% Cr, 11.4% Ni, 0.1% Al, 44 ppm of O and 127 ppm of S, with a density in the liquid state of 6943 kg/m^3, and three mold fluxes A_1, A_2, and A_3. The basicity of the powders is the same, (%CaO)/(%SiO$_2$) = 0.7, the density of the first two powders is 2540 kg/m^3, and the last one has a density of 2530 kg/m^3. The viscosities of the powders A_1, A_2, and A_3 are 0.3, 0.7, and 1.1 Pa-s, respectively, and their interfacial tensions in contact with steel 305 are 755 ± 70, 632 ± 80, and 883 ± 100 mN/m, respectively. The last two powders have 5 and 11 mass % of Al$_2$O$_3$. The calculation of the critical velocity for flux entrainment is straightforward using the following Equation [28]:

$$V_{cr} = 3.065 \left(\frac{\sigma_{m-s}^{0.292} g^{0.115}}{h_s^{0.365}} \right) \left[\frac{(\rho_m - \rho_s)^{0.215}}{\rho_s^{0.695}} \right] \left(\frac{\mu_s^{0.231}}{\mu_m^{0.043}} \right) \quad (7)$$

The maximum velocities at each time identified in the velocity profiles of the right port are plotted in Figure 4c and compared with the critical velocities calculated with Equation (7), assuming a standard flux layer thickness of 10 mm. The three horizontal lines labeled as A_1, A_2, and A_3 correspond to the critical velocities using the fluxes presented in the precedent lines.

From the velocities results in Figure 4c, it is evident that powder A_3 is the most suitable since most of the velocity peaks of the liquid are below this critical velocity corresponding to this powder.
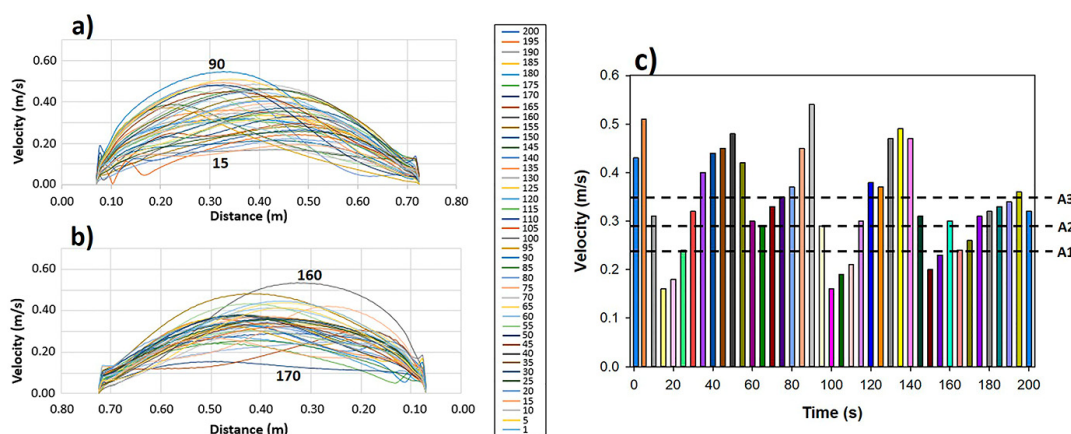

Figure 4. Velocities calculated along a line located 20 mm below the meniscus by the mathematical model: (**a**) right port, (**b**) left port. (**c**) Comparison of meniscus velocities with critical velocities to induce powder entrainment.

To complement the information about the unsteady nature of the fluid flow in the mold provided in Figure 4a,b and Figure 5a–f shows the numerical velocity fields in the mold's central plane of symmetry at different times. Twenty seconds after starting the time count, the flow looks very symmetric; sixty seconds later, both jets flow down the mold, and the loss of symmetry begins. After another sixty seconds, in Figure 5c, the

flow is asymmetric, and the upper roll flow on the right side is more developed than the upper roll flow on the left. In Figure 5d, the flow comes back to a symmetric flow pattern during the next sixty seconds. Figure 5e shows a loss of flow symmetry sixty seconds after the generation of the last symmetric flow, but it is rapidly recovered after a few seconds (following periods of 14 s). The upper roll flow on the left side advances unevenly than the upper jet on the right side. Forty seconds later, in Figure 5f, the flow symmetry is recovered. Therefore, for 280 s, almost five minutes, the flow loses its symmetry twice, though the overall double roll flow pattern is always present. For the flow control standards generally observed in slab molds, the flow provided by this nozzle is considered stable. The loss of symmetry is due to requirements of maintaining the turbulent kinetic energy balance: the dissipation rate of kinetic energy takes place just on the wall and the production of the kinetic energy is located just some mm from the wall. Other terms, such as pressure and viscous transportation of kinetic energy, complement the total balance. When the system starts kinetic energy part of this energy is released to keep the energy balance resulting in the loss of symmetry. It is noteworthy to underline that those higher velocities in the meniscus ensure a rapid melting of the mold flux and that using the flux A_3 will avoid excessive powder entrainment.
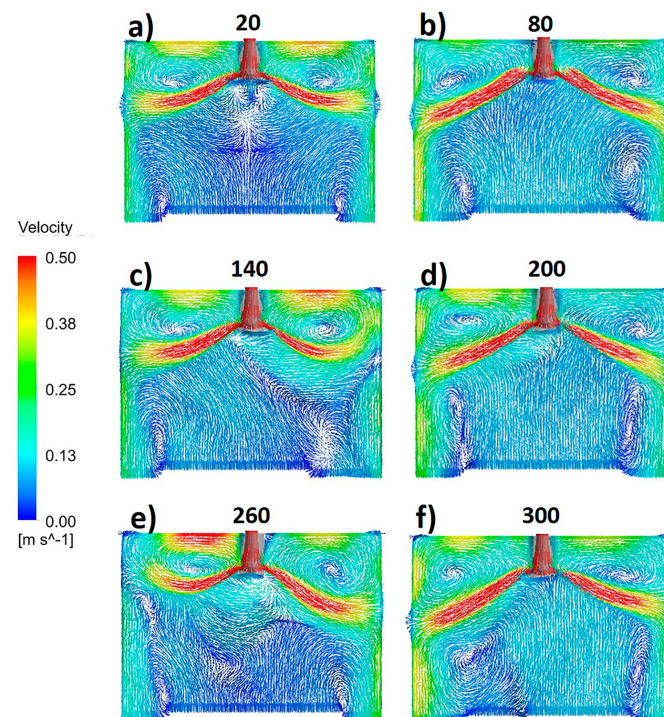

Figure 5. Numerical velocity fields in the central plane of the mold at different times ((**a**) 20 s; (**b**) 80 s; (**c**) 140 s; (**d**) 200 s; (**e**) 260 s; (**f**) 300 s) are indicated in each image.

The design of this nozzle develops a thin sublaminar boundary layer, δ_l, of variable thickness in its the interior wall [29]:

$$\delta_l = 5\frac{\nu}{v_*} \quad , \tag{8}$$

where $v_* = \sqrt{\frac{\tau_w}{\rho}}$ is the velocity friction and τ_W is the wall's strain-stress. This nozzle develops a thin sublaminar boundary thickness of about 10 µm along most of its interior wall. However, close to the port, the thickness increases well above 100 µm due to the boundary layer separation phenomenon, originated by the sudden change of the flow direction through the ports. The uniformity of the boundary layer thickness along the body of the nozzle leads to a plug-flow of the liquid, see Figure 6a. The expansions and

contractions of the cross-section areas of the nozzle give origin to plug-like flows of high and low velocities. The rounded corners of the upper side of the port avoid the severe flow separations in the boundary layer in these regions. A source of flow instability is the asymmetric flow formed by the closed area of the SGV as seen in the longitudinal-transversal view perpendicular to the plane of the ports, Figure 6b. The flow is biased inside of the nozzle because of the higher velocities through the open area of the SGV, leaving a stagnant region in the upper right zone, just beneath the closed area. The design of this nozzle consisting of expansions and contractions of the cross-section flow area helps to decrease the flow-biased characteristics. These flow control features help to straighten the stream coming from the tundish making a contribution to stabilize the meniscus in the mold. This design is different from other nozzle designs consisting of simple straight tubes. However, there is a recirculating flow in the bottom due to the presence of a low pressure-region generating and unfilled volume. Figure 6c,d shows the velocity fields in the right port in two planes; the first is in the central longitudinal axis of the pipe (PT1), and the second is just the outer frame of the port (PT3). Backflows occupy a proportion of the flow area of the port in the axial plane. The liquid flows through the upper left corner in Figure 6c; this area is larger in the outer plane of the port, see Figure 6d. The fluid leaves the nozzle through the outer frame of the port by a biased flow oriented toward its lower-left corner. The upper left corner is close to characteristics of stagnant conditions, leaving a reduced area utilization for liquid flowing into the mold. Figure 6e,f show the corresponding velocity fields in the axial and outer frame of the left port, respectively. In the left port, the backflows are a mirror image of those found in the right one. The fluid leaves the nozzle through the outer frame by a biased flow oriented in the lower right corner. Therefore, the source of flow instability is the biased flow inside the nozzle prevailing in both ports. It explains the low frequency of periodic-asymmetric flows despite the uniform boundary layer thickness throughout the interior wall of the nozzle.
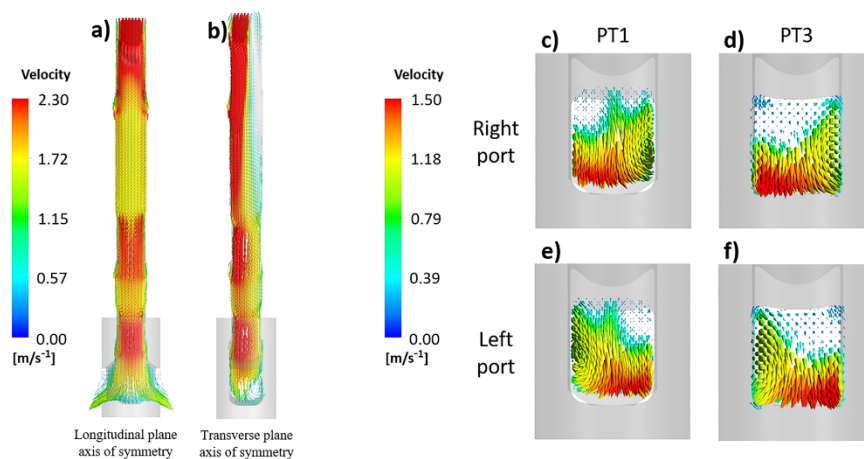

Figure 6. Numerical velocity fields in the nozzle: (**a**) longitudinal plane axis of symmetry, (**b**) transverse plane axis of symmetry. (**c**) Flow in the central plane of the internal axis of symmetry through the right port. (**d**) Flow through the outer port plane of the right port. (**e**) Flow in the central plane of the internal axis of symmetry through the left port. (**f**) Flow through the outer port plane of the left port.

Figure 7a shows the probability density function (PDF) of the measured velocities in the region of maximum velocity (located at 0.33 m from the mold's narrow face, labeled as L33) during a period of flow instability. The overall PDF is divided into two PDFs of positive and negative velocities, indicating the generation of backflows toward the narrow wall. In contrast, Figure 7b shows the PDF of positive velocities close to the nozzle (located at 0.60 m from the nozzle's wall, labeled as L60). The meaning of this later velocity PDF in the region adjacent to the nozzle is the permanent existence of a flow-oriented toward the nozzle. Figure 7c shows the velocity profile along with the distance between the narrow face and the nozzle's wall. The gray region in Figure 7c shows the standard deviation of velocities, and the green curve

is the average velocity profile. The regions close to the narrow face and the nozzle remain permanently, with small and positive velocities. The interpretation of the flow structure is feasible through the autocorrelation function, defined as:

$$R_{xx}(\tau) = \frac{1}{N} \sum X_i X_{i=j} \tag{9}$$

Normalized by $R_{xx}(0) = 1$. From the Schwartz inequality, $R_{xx} < 1$ for all $\tau \neq 0$; physically, the autocorrelation function expresses the correlation between the velocities at a time t and at other times $(t + \Delta t)$. Figure 8b shows the autocorrelations at the distance of 0.33 m (L33), and 0.60 m (L60) from the narrow mold's face, corresponding to the high turbulence regions and closer to the nozzle, respectively. The position L33 yields a fast-decreasing autocorrelation to 0.2 after seven seconds and to 0.6 at position L60 after 65 s. These differences explain the different velocity PDFs for both positions, as seen in Figure 7a,b.
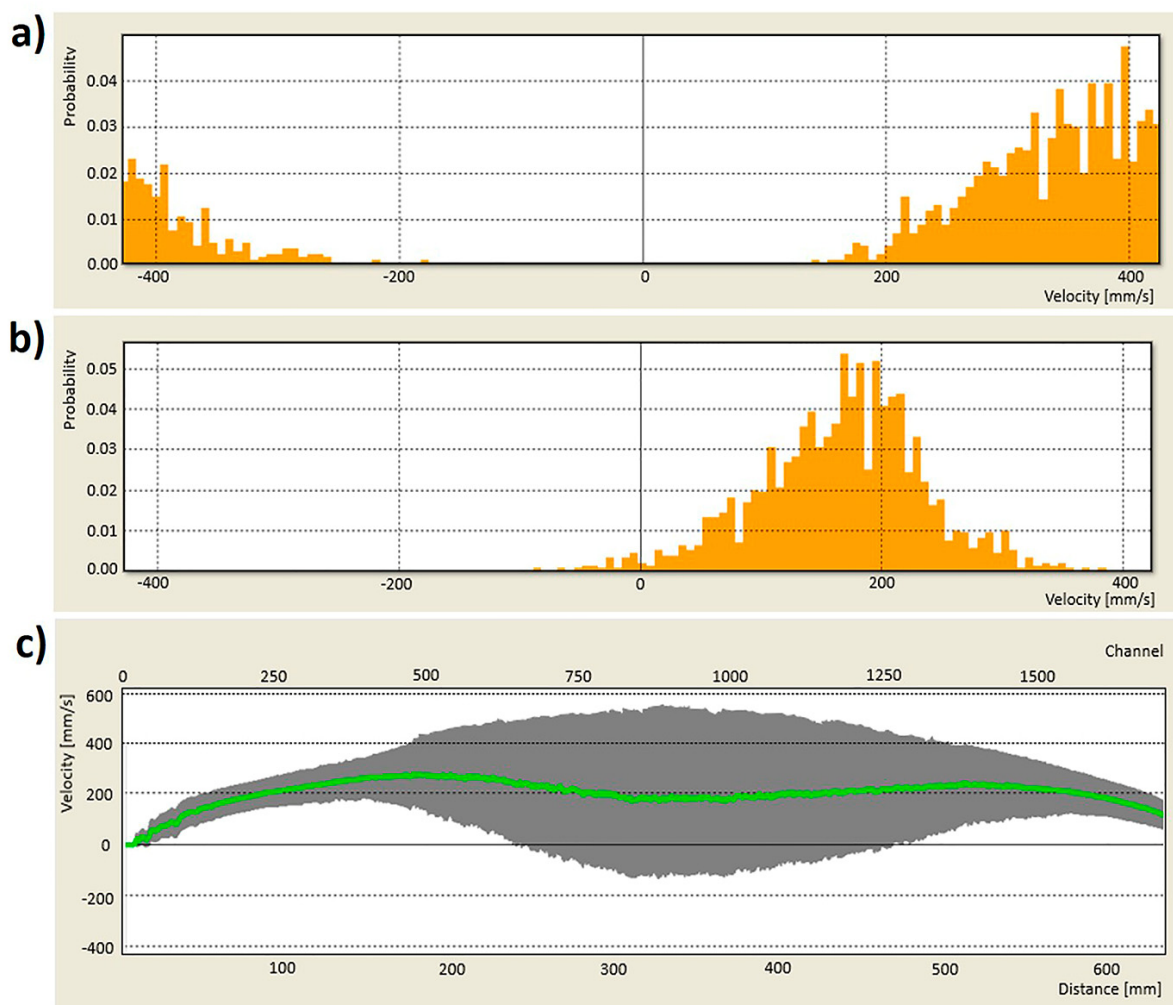
Figure 7. Turbulence features. (**a**) PDF of velocity in point L33. (**b**) PDF of velocity in point L60. (**c**) measured velocity profile along the line located 20 mm below the meniscus.
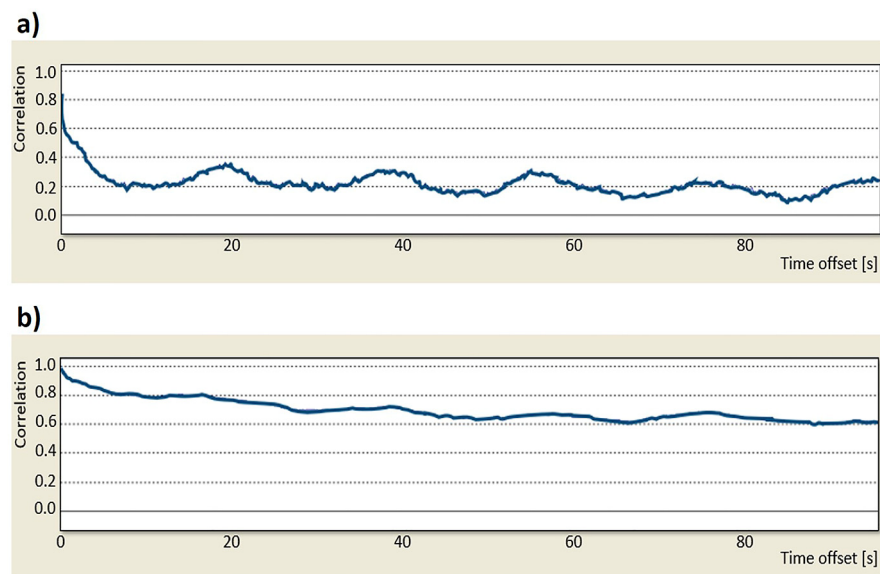
a)

b)

Figure 8. Autocorrelation of velocities: (**a**) at point L33, (**b**) at point L60.

5. Conclusions

A commercial nozzle delivers steel flows into a slab mold yielding reasonable turbulence control and stability of the flux-metal interface. Physical and mathematical models help unveil the nozzle design effects on fluid flow in the confined mold's space. From the results obtained using these modeling tools, the following conclusions can be drawn:

- The variations of bath levels during the casting are highly correlated, especially at both sides of the nozzle, and between the mold's narrow face and the nozzle's wall.
- The maximum velocity at the meniscus, recorded by the physical and mathematical models, is 0.55 m/s, which is well above the maximum velocity recommended to avoid flux entrainment into the liquid metal.
- An appropriate selection of the mold flux provides the possibility of casting sticking-breakout steels without intensive flux entrainment. A hot meniscus ensures effective flux melting, helping to eliminate problems of flux infiltration between the mold hot-face and the strand.
- The flow field of liquid in the mold yields low-frequency instabilities, though the double-roll flow is permanent. The origin of flow instabilities inducing asymmetric flows is the biased flow of steel in the nozzle due to the uneven opening of the slide gate valve.
- The turbulence shows high intensity in the upper roll flow at an intermediate position between the mold's narrow face and the nozzle.

Author Contributions: Project administration, C.R.M.-V.; Software, M.G.G.-S., J.G. and A.N.B.; Supervision, R.D.M.; Validation, J.G. All authors have read and agreed to the published version of the manuscript.

Conflicts of Interest: On behalf of all authors, the corresponding author states that there are no conflict of interest.

Nomenclature

C	Constants
g	Gravity constant
h	Slag thickness (mm)
k	Kinetic energy
p	Pressure (Pa)
S	Mean rate of strain tensor (s^{-1})
t	Time (s)
u	Velocity magnitude (m/s)
V	Velocity (m/s)
Greek letters	
δ	Delta function
ε	Turbulent dissipation rate (m^2/s^3)
η	Effectiveness factor (dimensionless)
μ	Dynamic viscosity (Pa^{-s})
ν	Viscosity (Pa^{-s})
ρ	Density (kg/m^3)
σ	Surface tensión and turbulent Prandtl number
τ	Stress tensor
Sub-indexes	
cr	Critical
m	Metal
R	Reynolds
s	Slag
t	Turbulent
w	Wall
xx	Autocorrelation

References

1. Suni, J.P.; Henein, H. Analysis of shell thickness irregularity in continuously cast middle carbon steel slabs using mold thermocouple data. *Metall. Mater. Trans. B* **1996**, *27*, 1045–1056. [CrossRef]
2. Bradi, A.; Natarajan, T.T.; Snyder, C.C.; Powers, K.D.; Mannion, F.J.; Cramb, A.W. A mold simulation for the continuous casting of steel: Part I. The development of a simulator. *Metall. Mater. Trans. B* **2005**, *36*, 355–371.
3. Yamamura, H.; Yamasaki, N.; Kajitani, T.; Mineta, S.; Nakashima, J. *Clarification and Control of the Heat Transfer Phenomenon in the Mold and Strand of Continuous Casting Machines*; Technical Report No. 104; Nippon Steel: Tokyo, Japan, 2013; pp. 54–61.
4. Yin, H.B.; Yao, M. Analysis of the non-uniform slag film, mold friction and the new cracking criterion for round billet continuous casting. *Metall. Mater. Trans. B* **2005**, *36*, 857–864. [CrossRef]
5. Kajitani, T.; Kato, Y.; Harada, K.; Saito, K.; Harashima, K.; Yamada, W. Mechanism of a hydrogen induced sticker breakout in continuous casting of steel: Influence of hydroxyl ions in mould flux on heat transfer and lubrication in the continuous casting mould. *ISIJ Int.* **2008**, *48*, 1215–1224. [CrossRef]
6. Hu, P.; Wang, X.; Wei, J.; Yao, M.; Guo, Q. Investigation of liquid/solid slag and air gap behavior inside the mold during continuous slab casting. *ISIJ Int.* **2018**, *58*, 892–898. [CrossRef]
7. Zhang, X.G.; Zhang, W.X.; Jin, J.Z.; Evans, J.W. Flow of steel in mold region during continuous casting. *J. Iron Steel Res. Int.* **2007**, *14*, 30–35. [CrossRef]
8. Feng, S.; Hong, L.X.; Wang, B.; Liu, S.; Yang, Z.; Feng, K.; Zhang, J. Numerical Study of Flow Behavior and Optimization of Nozzle Ports in Continuous Casting Slab Mold. In *CFD Modeling and Simulation in Materials Processing*; Springer: Berlin/Heidelberg, Germany, 2016; pp. 255–261.
9. Gupta, D.; Lahiri, A.K. A water model study of the flow asymmetry inside a continuous slab casting mold. *Metall. Mater. Trans. B* **1996**, *27*, 757–764. [CrossRef]
10. Wang, Y.D.; Zhang, L.F.; Yang, W.; Ren, Y. Effect of nozzle type on fluid flow, solidification, and solute transport in mold with mold electromagnetic stirring. *J. Iron Steel Res. Int.* **2021**, 1–10. [CrossRef]
11. Yokoya, S.; Takagi, S.; Iguchi, M.; Marukawa, K.; Hara, S. Swirling flow effect in immersion nozzle on flow in slab continuous casting mold. *ISIJ Int.* **2000**, *40*, 578–583. [CrossRef]
12. Yang, H.; Zhang, X.Z.; Deng, K.; Li, W.; Gan, Y.; Zhao, L. Mathematical simulation on coupled flow, heat, and solute transport in slab continuous casting process. *Metall. Mater. Trans. B* **1998**, *29*, 1345–1356. [CrossRef]
13. Gan, M.; Pan, W.; Wang, Q.; Zhang, X.; Pinghe, S. Effect of exit shape of submerged entry nozzle on flow field and slag entrainment in continuous casting mold. *Metall. Mater. Trans. B* **2020**, *51*, 2862–2870. [CrossRef]

14. Miki, Y.; Takeuchi, S. Internal defects of continuous casting slabs caused by asymmetric unbalanced steel flow in mold. *ISIJ Int.* **2003**, *43*, 1548–1555. [CrossRef]

15. Naijat, F.M.; Thomas, B.G.; Hershey, D.E. Numerical study of steady turbulent flow through bifurcated nozzles in continuous casting. *Metall. Mater. Trans. B* **1995**, *26*, 749–765.

16. Iguchi, M.; Yoshida, J.; Shimizu, T.; Mizuno, Y. Model study on the entrapment of mold powder into molten steel. *ISIJ Int.* **2000**, *40*, 685–691. [CrossRef]

17. Nakato, H.; Saito, K.; Oguchi, Y.; Namura, N.; Sorimachi, K. *70th Steel Conference Proceedings: Pittsburgh Meeting, 29 March–1April 1987*; The Iron and Steel Society: Pittsburgh, PA, USA, 1987; pp. 427–431.

18. Thomas, B.G. Modeling of continuous-casting defects related to mold fluid flow. *Iron Steel Technol.* **2006**, *3*, 127–141.

19. Striedinger, R.; Sancho, L.F.; Díaz, J.; De Santis, M.; Ridolfi, M.R.; Poli, A.; Bennani, A.; Laraudogoitia, J.; Ciriza, J.; Holzhauser, J.; et al. *Enhanced Steel Product Quality and Productivity through Improved Flux Performance in the Mould by Optimizing the Multiphase Flow Conditions and with Special Regard to Melting and Entrapment*; European Commission Research Fund for Coal and Steel: Brussels, Belgium, 2007.

20. Jalali, P.N.; López, P.E.R.; Nilsson, C.; Hietanen, P.; Jönsson, P. Diagnosis and optimization of continuous casting practices through numerical modelling. *Metall. Ital.* **2016**, *108*, 43–49.

21. Hagemann, R.; Schwarze, R.; Heller, H.P.; Scheller, P. Model investigations on the stability of the steel-slag interface in continuous-casting process. *Metall. Mater. Trans. B* **2013**, *44*, 80–90. [CrossRef]

22. Calderón-Ramos, I.; Morales, R.D. Influence of turbulent flows in the nozzle on melt flow within a slab mold and stability of the metal-flux interface. *Metall. Mater. Trans. B* **2016**, *47*, 1866–1881. [CrossRef]

23. Cui, H.; Zhang, K.; Wang, Z.; Chen, B.; Liu, B.; Qing, J.; Li, Z. Formation of surface depression during continuous casting of high-Al TRIP steel. *Metals* **2019**, *9*, 204. [CrossRef]

24. Mills, K.C.; Fox, A.B.; Thackrav, R.P.; Li, Z. Performance and properties of mould fluxes. *Ironmak. Steelmak.* **2005**, *32*, 26–34. [CrossRef]

25. ANSYS Inc. *FLUENT 6.2, User's Guide, Centerra Resource Park 10 Cavendish Court Lebanon*; ANSYS Inc.: Canonsburg, PA, USA, 2005; p. 51.

26. Wilcox, D.C. *Turbulence Modeling for CFD*; D.C.W. Industries Inc.: La Cañada Flintridge, CA, USA, 2000; pp. 123–128.

27. Chung, T.J. *Computational Fluid Dynamics*; Cambridge University Press: London, UK; New York, NY, USA, 2002; pp. 106–119.

28. Cramb, A.W.; Chang, Y.; Harman, J.; Sharah, A.; Jimbo, J. *Proceedings of the 5th International Conference on Molten Slags, Fluxes, and Salts '97: 5–8 January 1997, Sydney, Australia*; The Society: Warrendale, PA, USA, 1996.

29. Gutiérrez, E.; de Barreto, J.J.; García-Hernández, S.; Morales, R.D.; González-Solórzano, M.G. Decrease of nozzle clogging through fluid flow control. *Metals* **2020**, *10*, 1420. [CrossRef]